

A Sensitive Broadband (UV–vis–NIR) Perovskite Photodetector Using Topological Insulator as Electrodes

Feng-Xia Liang, Lin Liang, Xing-Yuan Zhao, Lin-Bao Luo,* Yu-Hung Liu, Xiao-Wei Tong, Zhi-Xiang Zhang, and J. C. Andrew Huang*

Here, a sensitive and broadband perovskite photodetector is developed by using crystalline topological insulator (TI) Bi_2Se_3 film as the electrode, which is synthesized by molecular beam epitaxy (MBE). The as-fabricated $\text{Bi}_2\text{Se}_3\text{-FA}_{0.85}\text{Cs}_{0.15}\text{PbI}_3\text{-Bi}_2\text{Se}_3$ photodetector exhibits apparent sensitivity to 650 nm illumination with an on/off ratio of 0.8×10^5 and good reproducibility. The responsivity, external quantum efficiency, and specific detectivity are estimated to be 8.4 A W^{-1} , 1604%, and 1.7×10^{13} Jones, respectively, which are better not only than the perovskite device using Au as electrode, but also than the majority of other perovskite materials based devices. It is also interesting to find that the TI based perovskite photodetector displays obvious photoresponse to near infrared light (NIR) with 980 nm due to contribution of TI Bi_2Se_3 layer. It is believed that the present TI based perovskite photodetector holds promise for broadband and high-performance optoelectronic applications in the future.

1. Introduction

Photodetectors that can convert photons into electrical signal have sparked worldwide research interest lately for their significant applications in optical communication, imaging, safety monitoring, and biological sensing.^[1–6] The organic–inorganic hybrid perovskites are ideal photoelectric materials for assembling sensitive photodetector owing to their remarkable optical and electrical properties. Up to now, many efforts

have been devoted to developing various photodetectors based on a number of perovskite materials with different geometries.^[7–10] Among the various device components, the electrode material plays an important role in influencing the device performance in that the interfaces between electrode and semiconductor materials may determine the carrier injection efficiency.^[11] Traditional noble metals such as platinum (Pt), gold (Au), and silver (Ag) are commonly used as electrodes. However, the devices using noble metal as electrode usually suffer from considerable dangling bonds and irregular surfaces, which may lead to severe carrier scattering and impede the transport of charge carriers.^[12,13] Indium tin oxide (ITO) and graphene are another class of electrodes frequently employed in high-performance

photodetectors and the device based on these two materials still have some drawbacks, e.g., insufficient flexibility and poor near infrared light (NIR) transmittance for ITO^[14,15] and complicated fabrication and transfer process for graphene.^[16–18] By this token, it is imperative to find alternative electrode materials to achieve high-performance photodetectors.

Topological insulators (TIs, e.g., Bi_2Se_3 ,^[19] Bi_2Te_3 ,^[20] and Sb_2Te_3 ^[21]) have recently gained much attention for their exotic properties, which are characterized by insulating gap in bulk and time reversal symmetry protected gapless Dirac-type edge on the boundary. The joint presence of semiconductor properties in bulk and spin momentum locked metallic properties at surface make TI a promising building block for fabricating various optoelectronic devices including photodetector,^[22,23] field-effect transistors,^[24,25] and laser.^[26,27] In addition, TI has also demonstrated to be superior electrode for its topologically protected highly conductive surface channels, which can effectively suppress undesirable charge scattering. Recently, several intriguing works have been reported on the synthesis and application of high quality TI electrodes.^[11,15,28] For example, a novel broadband transparent topological insulator Bi_2Se_3 grid network was synthesized through a facile van der Waals epitaxy approach, enabling the potential use in the future electronic and optoelectronic devices.^[15] Additionally, the choice of Bi_2Te_3 as a carrier collection layer and photosensitive layer, an ultra-broadband $\text{Bi}_2\text{Te}_3/\text{Si}$ heterojunction photodetector from 370 nm to 118 μm was achieved.^[29] Very recently, using Bi_2Te_3 as electrode, all layered 2D $\text{Bi}_2\text{Te}_3\text{-SnSe-Bi}_2\text{Te}_3$ photodetector with very good device performance was achieved. The responsivity

Dr. F.-X. Liang, L. Liang, X.-Y. Zhao
School of Materials Science and Engineering
Anhui Provincial Key Laboratory of Advanced
Functional Materials and Devices
Hefei University of Technology
Hefei, Anhui 230009, China

Prof. L.-B. Luo, X.-W. Tong, Z.-X. Zhang
School of Electronic Science and Applied Physics and Anhui
Provincial Key Laboratory of Advanced Materials and Devices
Hefei University of Technology
Hefei, Anhui 230009, China
E-mail: luolb@hfut.edu.cn

Y.-H. Liu, Prof. J. C. A. Huang
Department of Physics
National Cheng Kung University
Tainan 701, Taiwan
E-mail: jcahuang@mail.ncku.edu.tw

The ORCID identification number(s) for the author(s) of this article can be found under <https://doi.org/10.1002/adom.201801392>.

DOI: 10.1002/adom.201801392

and detectivity were 5.5 A W^{-1} and 6×10^{10} Jones, respectively, much better than the previously reported SnSe photodetector.^[11]

In this article, a high-performance broadband perovskite photodetector was successfully fabricated by using crystalline TI Bi_2Se_3 film as electrode and $\text{FA}_{0.85}\text{Cs}_{0.15}\text{PbI}_3$ as photoelectric material. The as-fabricated device exhibits obvious sensitivity to 650 nm light illumination with good reproducibility. Optoelectronic analysis reveals that the main device parameters including responsivity, external quantum efficiency (EQE), on/off ratio, and detectivity are better not only than majority of other $\text{FA}_{0.85}\text{Cs}_{0.15}\text{PbI}_3$ based photodetectors, but also than the device that uses Au film as electrode. Further spectral photoresponse analysis finds that the Bi_2Se_3 TI based perovskite photodetector exhibits a relatively weak sensitivity to NIR (980 nm), which was mainly attributed to the contribution of photoelectric property of Bi_2Se_3 .

2. Results and Discussion

A schematic diagram of the TI based perovskite photodetector is presented in Figure 1a, in which a Cs-doped FAPbI₃ thin film was coated directly on two parallel Bi_2Se_3 thin films. The Bi_2Se_3 film is comprised of quintuple layers of Se-Bi-Se-Bi-Se along the *c* axis, which has two different forces, weak van der Waals interactions between each quintuple layer (QL) and strong covalent bonding within each QL.^[30,31] The detailed fabrication process is illustrated by a flowchart in Figure S1 in

the Supporting Information. Figure 1b shows a cross-sectional image of the as-fabricated device that is characterized by field emission scanning electron microscopy (FESEM). Because of obvious distinction in contrast, the three layers including perovskite, Bi_2Se_3 , and sapphire could be easily distinguished. The thickness of both perovskite film and Bi_2Se_3 are around 450 and 85 nm (Figure S2, Supporting Information), respectively. From the FESEM analysis shown in Figure 1c, one can easily find that the $\text{FA}_{0.85}\text{Cs}_{0.15}\text{PbI}_3$ has a continuous film with few pinholes and cracks. The X-ray diffraction (XRD) pattern of the $\text{FA}_{0.85}\text{Cs}_{0.15}\text{PbI}_3$ film is displayed in Figure 1d. In accordance with the reported literature, the main diffraction peaks with Cs doping level of 0.15 can be indexed to black phase of FAPbI₃.^[31] Figure 1e presents the XRD of the Bi_2Se_3 film, from which a series of (0 0 *n*) (*n* = 3, 6, 9, 12, 15, 18) diffraction peaks belonging to space group of $R\bar{3}m/D3\ 5d$ (JCPDS No. 89-2008) are observed. Besides, no other impurity phases appear in the XRD result, indicating high-crystalline quality of the molecular beam epitaxy (MBE)-grown Bi_2Se_3 film. The Raman spectrum of the Bi_2Se_3 film in Figure 1f contains three distinct characteristic peaks located at ≈ 67 , ≈ 126 , and $\approx 170 \text{ cm}^{-1}$, which can be attributed to an in-plane (*E*₂ *g*) and two out of plane (*A*₁ *1 g* and *A*₂ *1 g*) vibrational modes of the (-Se-Bi-Se-Bi-Se-) lattice, respectively.^[32] To study the composition and valance states of the Bi_2Se_3 film, X-ray photoelectron spectroscopy (XPS) analysis was performed. As exhibited in Figure 1g,h, two peaks at around 163.7 and 158.5 eV corresponding to the $4f_{5/2}$ and $4f_{7/2}$ spin orbit peaks are observed

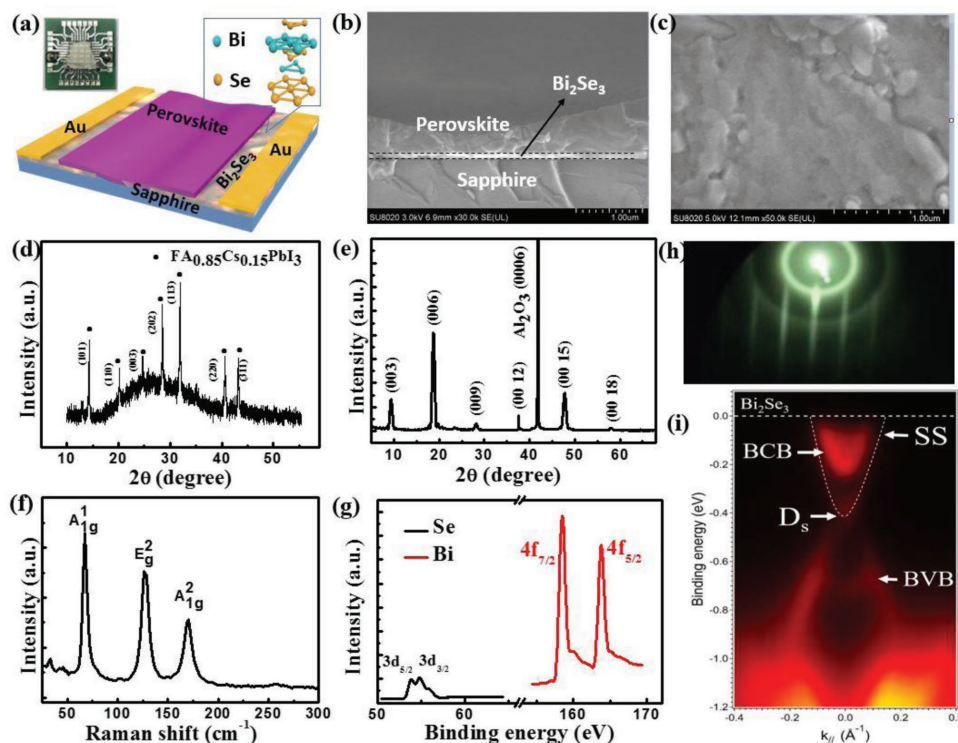


Figure 1. a) Schematic illustration of the Bi_2Se_3 - $\text{FA}_{0.85}\text{Cs}_{0.15}\text{PbI}_3$ - Bi_2Se_3 photodetector; the inset shows the crystal structure of the Bi_2Se_3 film and digital photograph of the device on PCB. b) Cross-sectional SEM image of the device. c) FESEM image of the perovskite thin film. d) XRD pattern of the $\text{FA}_{0.85}\text{Cs}_{0.15}\text{PbI}_3$ film. e) XRD pattern of the Bi_2Se_3 film on sapphire substrate. f) Raman spectrum of the Bi_2Se_3 film. g) The core-level spectra of Bi 4f and Se 3d. h) Typical reflection high-energy electron diffraction pattern of the Bi_2Se_3 film. i) Angle resolved photoemission spectrum of the Bi_2Se_3 film.

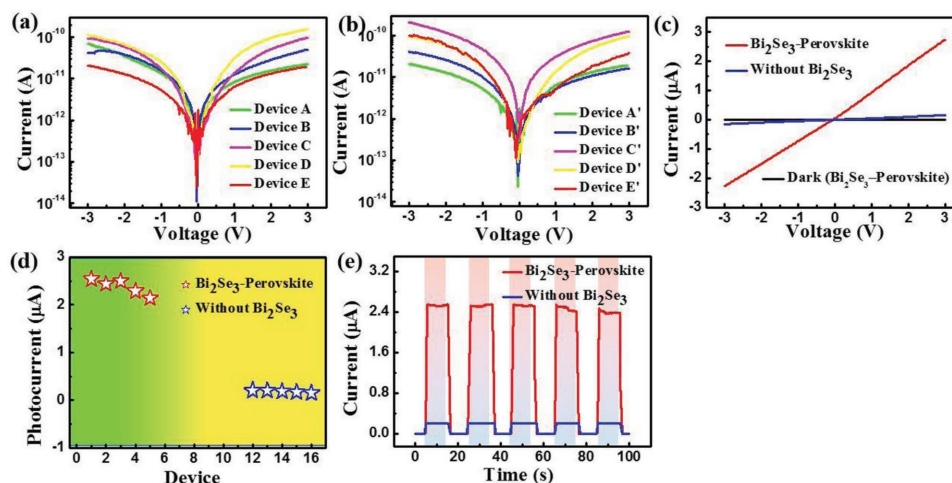


Figure 2. The five representative current–voltage characteristics in logarithmic scale in dark. a) With and b) without Bi₂Se₃ electrodes. c) *I*–*V* curves both in dark and light for the photodetector with and without Bi₂Se₃ electrodes. d) Comparison of the photocurrent for five representative devices with and without Bi₂Se₃ electrodes under 650 nm illumination. e) The temporal *I*–*t* curves for the device with and without Bi₂Se₃ electrodes, the devices were illuminated at 650 nm with an intensity of 63.7 mW cm⁻².

for oxidation state of Bi³⁺, whereas the other two peaks at 54.8 and 53.7 eV are attributed to the 3d_{3/2} and 3d_{5/2} orbital of divalent Se²⁻ ions, respectively. The reflection high-energy electron diffraction (RHEED) in Figure 1h displays a sharp streaky pattern, suggesting the single crystal of TI. According to the band mapping of the Bi₂Se₃ thin film (Figure 1i), the surface state bands with dispersion at the Γ point, forming a Dirac cone, correspond to the characteristic gapless surface state of Bi₂Se₃. The Dirac point is located at binding energy -0.4 eV. These results indicate that the present MBE derived Bi₂Se₃ sample has a high crystallinity.

Optoelectronic analysis reveals that the choice of Bi₂Se₃ TI as electrode is profitable for light detection. **Figure 2a,b** compares the *I*–*V* curves of two groups of devices with and without Bi₂Se₃ film, respectively. The nearly linear *I*–*V* characteristics in the dark for both devices corroborate that good Ohmic contact with negligible contact barrier forms at perovskite film/TI and perovskite/Au electrodes interfaces. The dark current of both groups are in the same order of magnitude (10⁻¹⁰–10⁻¹¹ A). When the device was illuminated by 650 nm light, the current increased abruptly for both devices (Figure 2c). This behavior has been confirmed by other five representative devices with good reproducibility as shown in Figure 2d. Figure 2e further displays the temporal response of two kinds of devices at 3 V at 650 nm with an intensity of 63.7 mW cm⁻². Both devices could be easily switched between high and low conduction states as the illumination was repeatedly switched on and off. Specifically, the photocurrent rises to 2.5×10^{-6} and 2.1×10^{-7} A for devices with and without Bi₂Se₃, respectively, yielding an on/off ratio of 0.8×10^5 and 0.9×10^4 , which means the Bi₂Se₃ electrode can increase both photocurrent and on/off ratio by nearly tenfold. It should be pointed that for this photodetector, the spacing between the Au electrode and perovskite region can also influence the photocurrent. As shown in Figure S3 in the Supporting Information, with the increase of the spacing, the photocurrent under 650 nm illumination is found to slightly decrease.

To shed light on the origin of the superior photoresponse properties in TI based device, the energy band diagram of Bi₂Se₃-FA_{0.85}CS_{0.15}PbI₃-Bi₂Se₃ photodetector under light illumination is plotted in **Figure 3**. Apparently, three factors are believed to contribute to photocurrent: 1) The perovskite material: When the device was illuminated by incident light with photon energy higher than the bandgap of perovskite (1.5 eV),^[33] electrons are excited to the lowest unoccupied molecular orbital (LUMO) while holes in the highest occupied molecular orbital (HOMO). As a result, the photo-generated carriers will transport quickly across the perovskite/TI interface to opposite directions due to external electric field.^[34] In fact, the transfer of carrier from perovskite to TI was verified by the quenched photoluminescence (PL) intensity of the perovskite layer/Bi₂Se₃ heterojunction, as shown in Figure S4 in the Supporting Information.^[35] 2) The interior of Bi₂Se₃: On account of the relatively small bandgap of Bi₂Se₃ interior (≈ 0.3 eV^[36]), electron–hole pairs can also be produced once illuminated by photons with energy larger than the bandgap of

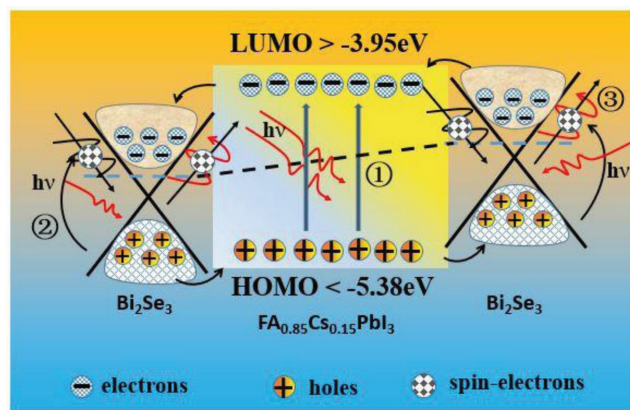


Figure 3. Energy band diagram of the Bi₂Se₃-FA_{0.85}CS_{0.15}PbI₃-Bi₂Se₃ photodetector under light illumination.

TI, but less than that of perovskite. This is in agreement with the apparent sensitivity to NIR light (980 nm). 3) The surface of Bi_2Se_3 : At equilibrium condition in darkness, a net charge flow (also called spin current) can form along the surface of Bi_2Se_3 TI. Once shined by the NIR light from LED source, the spin currents may be converted into polarized net charges, which may contribute to the photocurrent as well.^[22] Without question, the late two factors are responsible for the relatively good photoresponse of $\text{Bi}_2\text{Se}_3\text{-FA}_{0.85}\text{Cs}_{0.15}\text{PbI}_3\text{-Bi}_2\text{Se}_3$ in comparison with that of $\text{Au-FA}_{0.85}\text{Cs}_{0.15}\text{PbI}_3\text{-Au}$.

Further broadband photoresponse properties of the $\text{Bi}_2\text{Se}_3\text{-FA}_{0.85}\text{Cs}_{0.15}\text{PbI}_3\text{-Bi}_2\text{Se}_3$ photodetector in the range from ultraviolet (UV) to NIR were systematically studied. Figure 4a displays a set of I - V curves at different wavelengths from 365 to 980 nm under intensity of $386 \mu\text{W cm}^{-2}$. It can be seen that the peak photoresponse is centered at around 650 nm. The power dependent photocurrent at different wavelengths is plotted in Figure 4b. One can find that the photocurrent increases with the increase of light intensity at each wavelength, which is understandable as more photo-generated carriers are produced at stronger light intensity. From the spectral response in Figure 4c, it is obvious that the device exhibits a broadband sensitivity from UV to NIR light. Such a spectral selectivity is consistent with the adsorption spectrum of perovskite and Bi_2Se_3 in Figure 4d. For illumination at UV-vis region, most light is absorbed by perovskite before reaching Bi_2Se_3 electrode, thus perovskite makes a great contribution to the photocurrent. When the illumination was changed with NIR light, Bi_2Se_3 shows enhanced adsorption properties in comparison with

perovskite. In this case, the majority of the photocurrent is induced due to the photoconductive effect of Bi_2Se_3 electrode, as opposed to perovskite.

To quantify the superior performance of the $\text{Bi}_2\text{Se}_3\text{-FA}_{0.85}\text{Cs}_{0.15}\text{PbI}_3\text{-Bi}_2\text{Se}_3$ photodetector, we performed a series of photoresponse measurement at 650 nm under different light intensities. Figure 5a,b plot the I - V and I - t curves of the device under light intensity ranging from 1.66 to 63.7 mW cm^{-2} , respectively. The quantitative relationship between photocurrent and light intensity is presented in Figure 5c, which is described by a power law $I = AP^\theta$, where, I is the photocurrent, P is light intensity, and θ is an exponent determining the response of photocurrent to light intensity. Through fitting the I - P curves, θ is estimated to be 0.64. Such a relatively low value may be related to a consequence of the complicated process during electron-hole generation in the topological insulator and perovskite film upon 650 nm irradiation.^[37] Afterward, several important parameters such as the on/off ratio (I_λ/I_d) responsivity (R), detectivity (D), and EQE are calculated by the following equations^[38]

$$R = \frac{I_\lambda - I_d}{P_\lambda A} \quad (1)$$

$$D = \frac{RA^{1/2}}{(2eI_d)^{1/2}} \quad (2)$$

$$\text{EQE} = R \frac{hc}{e\lambda} \quad (3)$$

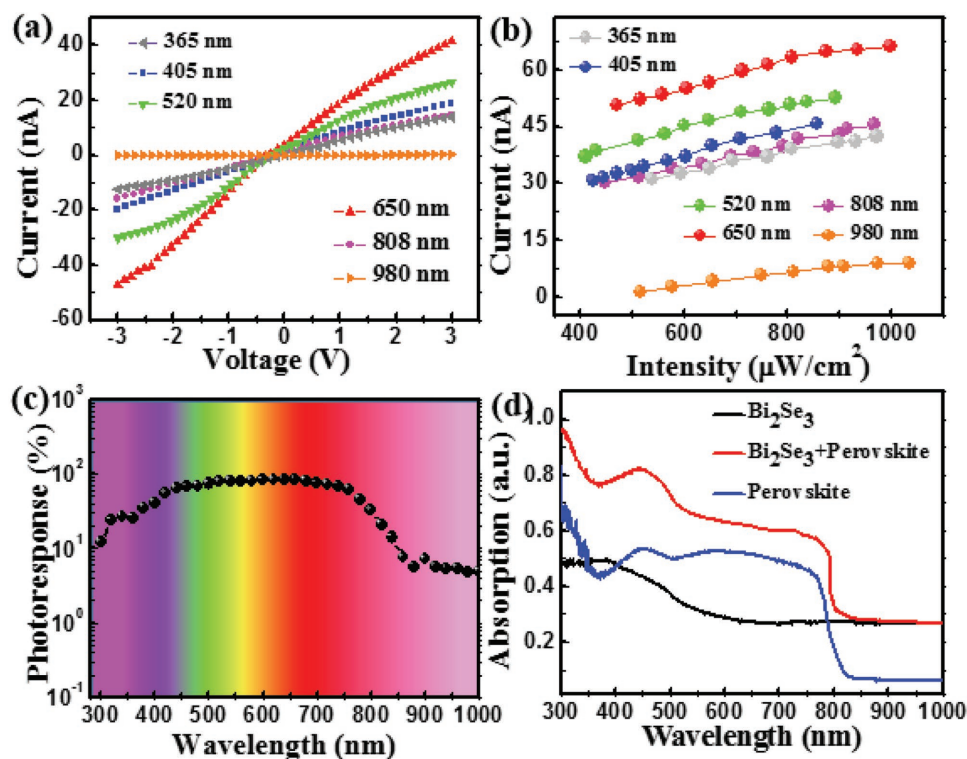


Figure 4. a) Voltage-dependent photocurrent upon illumination with different wavelengths, the power intensities are all $386 \mu\text{W cm}^{-2}$. b) Power-dependent photocurrent with different wavelengths. c) Normalized spectral response of the device in the range from 300–1000 nm. d) Absorption curve of Bi_2Se_3 , perovskite, and Bi_2Se_3 /perovskite hybrid.

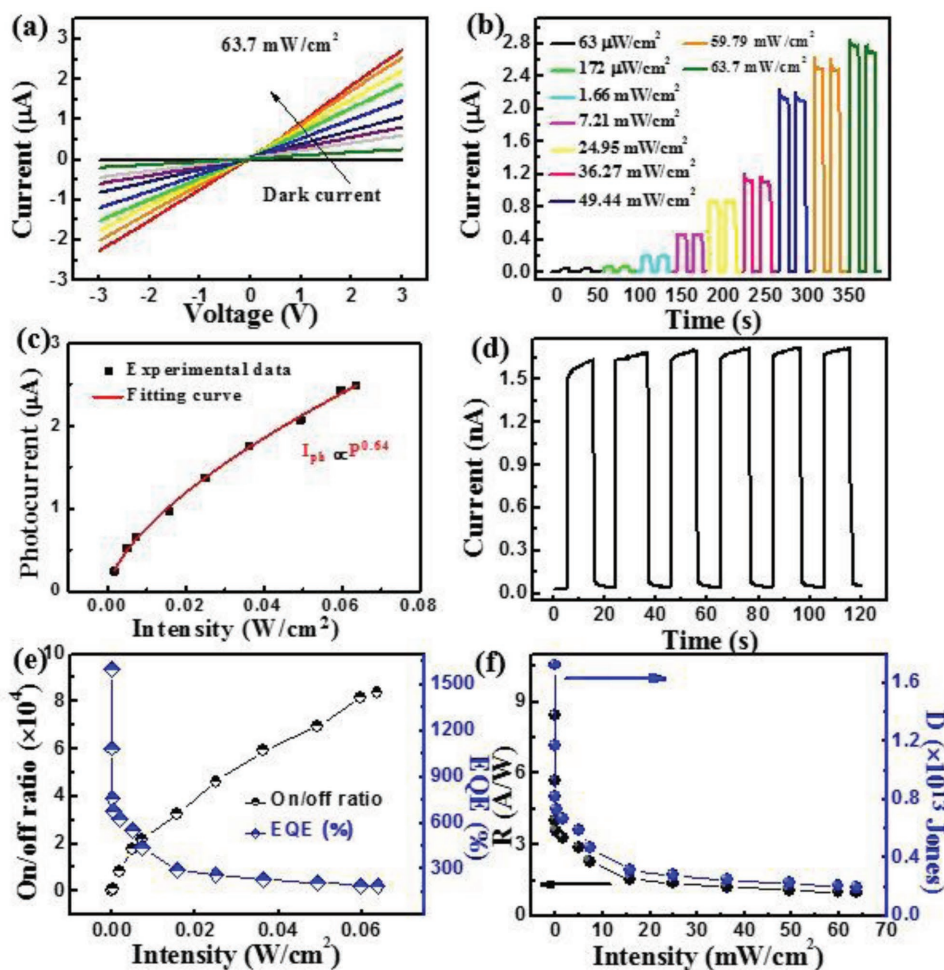


Figure 5. a) I - V curves of the photodetector at 650 nm with different light intensities. b) Temporal I - t curves under various light intensities at 650 nm. c) Photocurrent as a function of the light intensity at bias of 3 V. d) Temporal I - t curves with a light intensity of $4.8 \mu\text{W cm}^{-2}$ at 650 nm. e) On/off ratio and EQE of the device as a function of the light intensity. f) The dependence of responsivity and detectivity on light intensity at a bias of 3 V.

Here, R is the photocurrent generated every unit incident power, which can be figured out by the photocurrent (I_{ph}), dark-current (I_d), power density (P_{λ}), and active area of the device (A) in Equation (1). D is used to evaluate the capability of detecting weak signals, which can be determined by R , A , I_d , and

elemental charge (e) as described in Equation (2). EQE refers to the number of effective carriers generated per incident photon. It can be calculated by Equation (3), where h , c , and λ represent the Planck constant, light speed, and wavelength, respectively. Based on these equations, the power dependent on/off ratio,

Table 1. Comparison of device performance of our device and other perovskite based photodetectors with different electrodes.

Device	R [A W^{-1}]	EQE [%]	D [Jones]	$I_{\text{light}}/I_{\text{dark}}$	Wavelength [nm]	Ref.
$\text{Bi}_2\text{Se}_3\text{-FA}_{0.85}\text{Cs}_{0.15}\text{PbI}_3\text{-Bi}_2\text{Se}_3$	8.4	1604	1.7×10^{13}	0.8×10^5	650	Our work
$\text{Au-FA}_{0.85}\text{Cs}_{0.15}\text{PbI}_3\text{-Au}$	2.5	477	5.1×10^{12}	0.9×10^4	650	Our work
ITO-MAPbI ₃ -ITO	3.49	1190	—	324	365	[39]
Au-CsPbBr ₃ -Au	34	$\approx 10^4$	7.5×10^{12}	—	442	[40]
ITO-MAPbI ₃ -Au	0.418	—	1.2×10^{13}	58	White light	[41]
$\text{Ag-MA}_{0.5}\text{FA}_{0.5}\text{Pb}_{0.5}\text{Sn}_{0.5}\text{I}_3\text{-Ag}$	>0.1	43	$>1 \times 10^{12}$	—	NIR	[42]
ITO-MAPbCl ₃ -ITO	18	100	1×10^{12}	—	385	[43]
Au-MAPbI _{3-x} Cl _x -Au	—	—	1.3×10^{12}	$>2.1 \times 10^4$	671	[44]
$\text{Ag-(FASnI}_3\text{)}_{0.6}\text{(MAPbI}_3\text{)}_{0.4}\text{-FTO}$	0.4	>65	1.2×10^{12}	—	900	[45]

EQE, R , and D are computed and plotted in Figure 5e,f, respectively. Apparently, all of the parameters except the on/off ratio are found to gradually decrease as light intensity increases. By employing a weak light intensity ($4.8 \mu\text{W cm}^{-2}$, Figure 5d), the maximum value of EQE, R , and D can be as high as 1604%, 8.4 A W^{-1} , and $1.7 \times 10^{13} \text{ cm Hz}^{1/2} \text{ W}^{-1}$, respectively (Please refer to the Supporting Information for the detailed calculation). Furthermore, the corresponding parameters of the Au/perovskite/Au are calculated according to the data presented in Figure S5 in the Supporting Information. **Table 1** summarizes the device performance of the perovskite photodetectors using different electrodes. Without doubt, the $\text{Bi}_2\text{Se}_3\text{-FA}_{0.85}\text{Cs}_{0.15}\text{PbI}_3\text{-Bi}_2\text{Se}_3$ presents much better device performance than the device composed of Au electrode. What is more, the key parameters of the present $\text{Bi}_2\text{Se}_3\text{-FA}_{0.85}\text{Cs}_{0.15}\text{PbI}_3\text{-Bi}_2\text{Se}_3$ device including R , D , and EQE are poor than the Au-CsPbBr₃-Au device, but are better than majority of other MAPbX₃ (X: Cl, Br, I) or FASnI₃ based photodetectors.^[39–45] From the transient photoresponse in the Figure S6 in the Supporting Information, the rise/decay

times of the heterojunction device are estimated to be 16/14 μs , respectively, which are comparable to other perovskite based photodetectors.

Although the sensitivity to illumination with wavelength longer than 850 nm/shorter than 400 nm is relatively weak, the photosensitivity is still strong enough for NIR/UV light detection. **Figure 6a** plots the detailed photoresponse characteristics under NIR illumination, in which a dramatic photocurrent increase with an on/off ratio of 10^2 is observed. Similarly, the photocurrent increases monotonously with the increasing voltage and intensity, as displayed in Figure 6b,c. Based on the obtained data, both R and D are further calculated and presented in Figure 6d. Specifically, the R and D are estimated to be 1.02 A W^{-1} and $2.08 \times 10^{12} \text{ Jones}$, respectively, at light intensity of $5.6 \mu\text{W cm}^{-2}$. To disclose the underlying reason behind this UV sensitivity, other two devices made of Au-Bi₂Se₃-Au and Au-perovskite-Au structures were fabricated for comparison. As shown in Figure 6e,f, the Au-Bi₂Se₃-Au photodetector has an obvious photoresponse with a photocurrent as

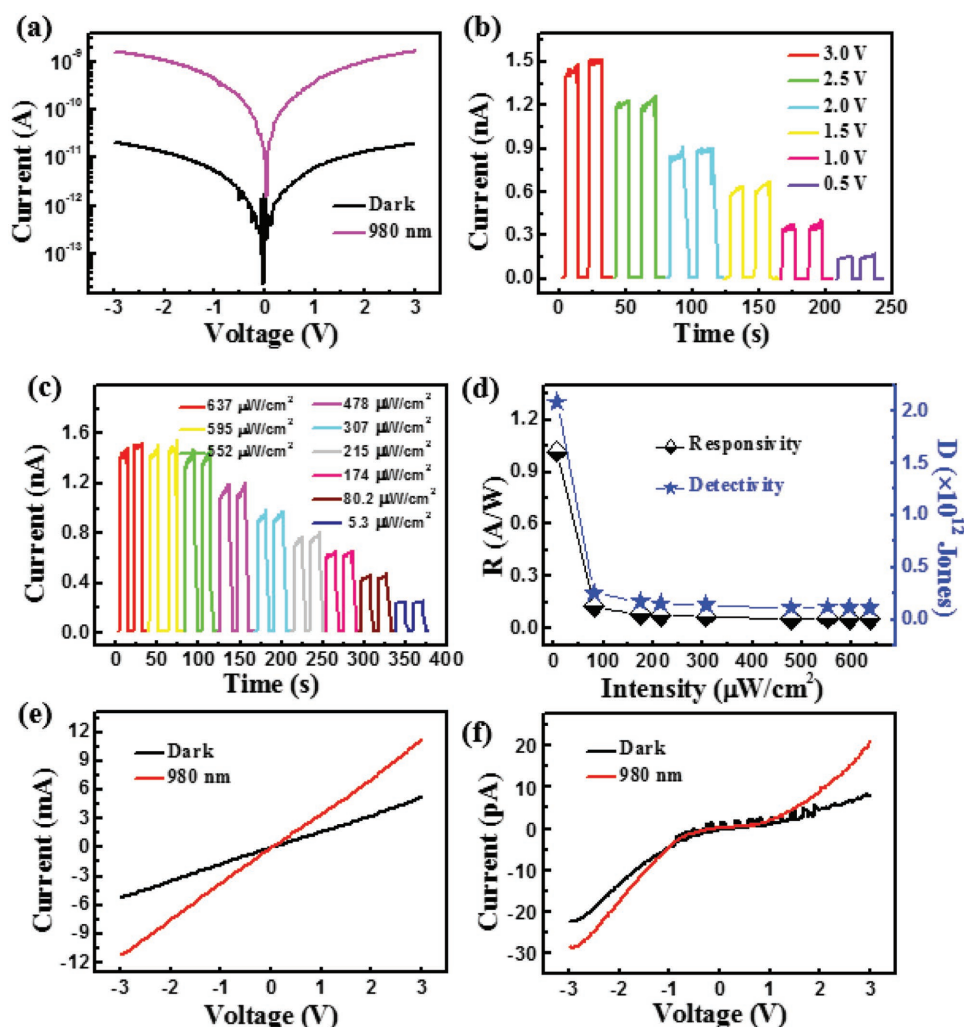


Figure 6. a) I - V curve with and without 980 nm illumination. b) Photoresponse of the device under different bias voltage. c) The temporal photoresponse at 980 nm with different light intensities. d) Both responsivity and detectivity under 980 nm light with different intensities. e) I - V characteristics of the Au-Bi₂Se₃-Au photodetector with and without 980 nm illumination. f) I - V characteristics of the Au-perovskite-Au photodetector with and without 980 nm illumination.

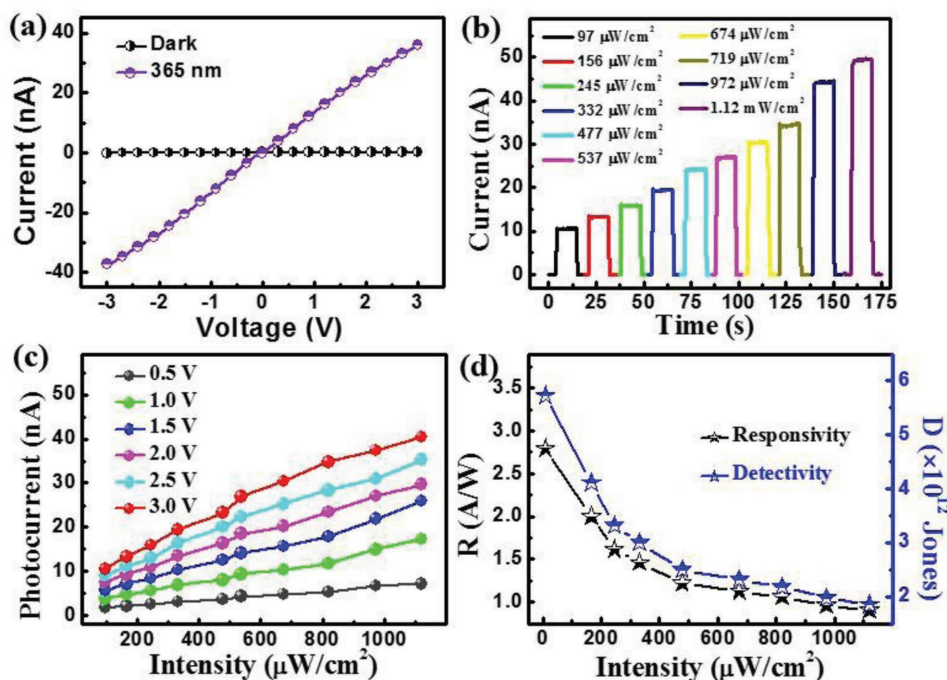


Figure 7. a) I - V curves with and without 365 nm illumination. b) The photoresponse to 365 nm with different intensities. c) The dependence of photocurrent on light intensity; the voltage was changed from 0.5 to 3.0 V. d) Both responsivity and detectivity under 365 nm illumination with different light intensities.

high as ≈ 11.19 mA, while the Au-perovskite-Au has neglectable response upon illumination at 980 nm. These results confirm that the photocurrent under 980 nm mainly stems from contribution of Bi_2Se_3 .

Similar sensitivity was observed in UV light region as well. Figure 7a shows the I - V curves of the Bi_2Se_3 - $\text{FA}_{0.85}\text{Cs}_{0.15}\text{PbI}_3$ - Bi_2Se_3 at UV light of 365 nm. The photocurrent is as high as 40.4 nA at 3 V, which is nearly 1.3×10^3 times higher than the dark current (2.97 pA). Further optoelectronic analysis finds that the photocurrent is determined by not only light intensity, but also bias voltage, as observed when NIR light was chosen as illumination source (Figure 7b,c). With the decrease in light intensity, both R and D will increase dramatically (Figure 7d). Specifically, at a weak UV light intensity of $8.1 \mu\text{W cm}^{-2}$, R and D are determined to be 2.8 A W^{-1} and 5.7×10^{12} Jones, respectively. These two values are slightly higher than that under NIR illumination. To further study the stability of the present perovskite photodetector, the device was stored in ambient condition for 3 months. Figure S7 in the Supporting Information compares both dark current and photocurrent as a function of storage duration. Obviously, the photocurrent decreased by 30–40%, while the dark current increased dramatically due to the relatively poor stability in air. As a matter of fact, such a relatively poor stability can be further improved by either encapsulating or surface engineering approaches.

3. Conclusion

In summary, a broadband photodetector assembled from $\text{FA}_{0.85}\text{Cs}_{0.15}\text{PbI}_3$ perovskite and TI Bi_2Se_3 film has been

demonstrated. The $\text{FA}_{0.85}\text{Cs}_{0.15}\text{PbI}_3$ perovskite was synthesized through a facile spin-coating process whereas the Bi_2Se_3 film by a molecular beam epitaxial method. The as-assembled device exhibits obvious photoresponse with peak sensitivity at 650 nm. The sensitivity is highly reproducible with a responsivity of 8.4 A W^{-1} . The corresponding external quantum efficiency, detectivity, and on/off ratio are estimated to be 1604%, 1.7×10^{13} Jones, and 0.8×10^5 , respectively.

4. Experimental Section

Materials Synthesis and Device Fabrication: The Bi_2Se_3 film was grown on sapphire (0006) substrate via MBE. High purity Bi (99.99%) and Se (99.99%) powders were evaporated from a Kundsén cell, with substrate temperature kept at 370°C for 33 min. The flux ratio of Bi:Se was maintained at 1:15 (\AA min^{-1}) during the film growth. The $\text{FA}_{0.85}\text{Cs}_{0.15}\text{PbI}_3$ perovskite film was prepared through a simple one-step spin-coating method. The precursor solution was first obtained by dissolving 461 mg of PbI_2 (Aldrich, 99%), 38.9 mg of CsI (Aldrich, 99.9%), and 145 mg of FAI (Aldrich, 99.5%) sequentially into a mixed solvent of 800 μL of N,N -dimethylformamide (DMF, 99.8%) and 200 μL of dimethyl sulfoxide (DMSO, >99.9%). To prepare the Bi_2Se_3 - $\text{FA}_{0.85}\text{Cs}_{0.15}\text{PbI}_3$ - Bi_2Se_3 photodetector, an opening window of $4 \times 10^{-5} \text{ cm}^2$ by photolithography was defined on the above as-synthesized topological insulator film. The channel length (L) and width (W) were 400 and 10 μm , respectively. Au metal electrode with thickness of around 50 nm was then deposited on the edge of the patterned Bi_2Se_3 film by the second photolithography combined with electron beam evaporation. Afterward, 20 μL of the as-prepared perovskite precursor solution was dropped on the patterned topological insulator electrode on sapphire substrate. The as-obtained perovskite film was sequentially annealed at 70°C for 2 min and 135°C for 10 min respectively. At last, the Bi_2Se_3 - $\text{FA}_{0.85}\text{Cs}_{0.15}\text{PbI}_3$ - Bi_2Se_3 photodetector was constructed as the color of the perovskite film changed to black-brownish.

Structural Analysis and Device Characterization: The morphology of the as-prepared films was characterized by an FESEM (Hitachi, SU8020) and atomic force microscopy (AFM, Benyuan Nanotech Com, CSPM-4000). Optical absorption was studied with a UV–vis spectrophotometer (UV-2550, Shimadzu, Japan). The phase composition of the as-prepared samples was recorded using an X-ray diffractometer (Rigaku D/max-rB). The XPS measurement of Bi₂Se₃ film was performed using a monochromatic Al K α source (1486.6 eV) produced by the XPS system. The Raman spectrum of Bi₂Se₃ was recorded on an HR Evolution (Horiba Jobin Yvon) Raman spectrometer with a 532 nm laser. The angle resolved photoemission spectroscopy (ARPES) experiments were performed at beamlines 21B1 of Taiwan Light Source in National Synchrotron Radiation Research Center (NSRRC). The MBE-grown Bi₂Se₃ covered with an Se capping layer was annealed at 180 °C about 1 h in an ultrahigh vacuum environment to remove the capping layer before ARPES measurements. The ARPES was measured in a ultrahigh vacuum chamber equipped with a hemispherical analyzer (Scienta R4000) with collecting angle $\pm 15^\circ$ at BL21B1 beamline in NSRRC. The spectrum was recorded at 80 K and base pressure 5×10^{-11} Torr with incident photon energy 20 eV.

The electrical measurement was conducted through a semiconductor characterization system (4200-SCS, Keithley Co. Ltd.), equipped with a monochromator (SP 2150, Princeton Co.). To study the optoelectronic properties, the laser diodes (Tanon Company, UV-100) with different wavelengths (365, 405, 520, 650, 808, and 980 nm) were adopted. The power intensity of the light sources was carefully calibrated by a power meter (Thorlabs GmbH, PM 100D) before measurement. All measurements were performed in air at room temperature.

Supporting Information

Supporting Information is available from the Wiley Online Library or from the author.

Acknowledgements

This work was supported by the National Natural Science Foundation of China (NSFC, Nos. 61575059, 61675062, and 21501038), the Fundamental Research Funds for the Central Universities (JZ2018HGXC0001), the National Science Council of Taiwan (NSC 100-2112-M-006-018-MY3) and the Open Foundation of Anhui Provincial Key Laboratory of Advanced Functional Materials and Devices (4500-411104/011).

Conflict of Interest

The authors declare no conflict of interest.

Keywords

detectivity, optoelectronic devices, perovskites, responsivity, topological insulators

Received: October 12, 2018
Revised: November 19, 2018
Published online: December 12, 2018

- [1] X. Gong, M. H. Tong, Y. J. Xia, W. Z. Cai, J. S. Moon, Y. Cao, G. Yu, C. L. Shieh, B. Nilsson, A. J. Heeger, *Science* **2009**, 325, 1665.
- [2] Y. J. Fang, Q. F. Dong, Y. C. Shao, Y. B. Yuan, J. S. Huang, *Nat. Photonics* **2015**, 9, 679.

- [3] Q. Q. Lin, A. Armin, P. L. Burn, P. Meredith, *Nat. Photonics* **2015**, 9, 687.
- [4] J. Lee, J. Kwon, E. Hwang, C. H. Ra, W. J. Yoo, J. H. Ahn, J. H. Park, J. H. Cho, *Adv. Mater.* **2015**, 27, 41.
- [5] L. T. Dou, Y. Yang, J. B. You, Z. R. Hong, W. H. Chang, G. Li, Y. Yang, *Nat. Commun.* **2014**, 5, 5404.
- [6] J. D. Yao, Z. Q. Zheng, G. W. Yang, *Adv. Opt. Mater.* **2017**, 5, 1600908.
- [7] M. I. Saidaminov, V. Adinolfi, R. Comin, A. L. Abdelhady, W. Peng, I. Dursun, M. J. Yuan, S. Hoogland, E. H. Sargent, O. M. Bakr, *Nat. Commun.* **2015**, 6, 8724.
- [8] H. Deng, X. K. Yang, D. D. Dong, B. Li, D. Yang, S. J. Yuan, K. K. Qiao, Y. B. Cheng, J. Tang, H. S. Song, *Nano Lett.* **2015**, 15, 7963.
- [9] V. Adinolfi, O. Ouellette, M. I. Saidaminov, G. Walters, A. L. Abdelady, O. M. Bakr, E. H. Sargent, *Adv. Mater.* **2016**, 28, 7264.
- [10] Z. X. Zhang, L. H. Zeng, X. W. Tong, C. Xie, Y. H. Tsang, L. B. Luo, Y. C. Wu, *J. Phys. Chem. Lett.* **2018**, 9, 1185.
- [11] J. D. Yao, Z. Q. Zheng, G. W. Yang, *Adv. Funct. Mater.* **2017**, 27, 1701823.
- [12] C. C. Chueh, M. Crump, A. K. Y. Jen, *Adv. Funct. Mater.* **2016**, 26, 321.
- [13] G. M. Berry, M. E. Bothwell, B. G. Bravo, G. J. Cali, J. E. Harris, T. Mebrahtu, S. L. Michelhaugh, J. F. Rodriguez, M. P. Soriaga, *Langmuir* **1989**, 5, 707.
- [14] H. L. Peng, W. H. Dang, J. Cao, Y. L. Chen, D. Wu, W. S. Zheng, H. Li, Z. X. Shen, Z. F. Liu, *Nat. Chem.* **2012**, 4, 281.
- [15] Y. F. Guo, M. Aisijiang, K. Zhang, W. Jiang, Y. L. Chen, W. S. Zheng, Z. H. Song, J. Cao, Z. F. Liu, H. L. Peng, *Adv. Mater.* **2013**, 25, 5959.
- [16] H. J. Tan, Y. Fan, Y. Q. Zhou, Q. Chen, W. S. Xu, J. H. Warner, *ACS Nano* **2016**, 10, 7866.
- [17] Y. M. Shi, K. K. Kim, A. Reina, M. Hofmanm, L. J. Li, J. Kong, *ACS Nano* **2010**, 4, 2689.
- [18] J. Mao, Y. Q. Yu, L. Wang, X. J. Zhang, Y. M. Wang, Z. B. Shao, J. S. Jie, *Adv. Sci.* **2016**, 3, 1600018.
- [19] H. Steinberg, D. R. Gardner, Y. S. Lee, P. Jarillo-Herrero, *Nano Lett.* **2010**, 10, 5032.
- [20] D. X. Qu, Y. S. Hor, J. Xiong, R. J. Cava, N. P. Ong, *Science* **2010**, 329, 821.
- [21] R. Venkatasubramanian, T. Colpitts, E. Watko, M. Lamvik, N. El-Masry, *J. Cryst. Growth* **1997**, 170, 817.
- [22] K. Zheng, L. B. Luo, T. F. Zhang, Y. H. Liu, Y. Q. Yu, R. Lu, H. L. Qiu, Z. J. Li, J. C. A. Huang, *J. Mater. Chem. C* **2015**, 3, 9154.
- [23] H. B. Zhang, X. J. Zhang, C. Liu, S. T. Lee, J. S. Jie, *ACS Nano* **2016**, 10, 5113.
- [24] F. K. Wang, L. G. Li, W. J. Huang, L. Li, B. Jin, H. Q. Li, T. Y. Zhai, *Adv. Funct. Mater.* **2018**, 28, 1802707.
- [25] J. D. Yao, Z. Q. Zheng, G. W. Yang, *J. Mater. Chem. C* **2016**, 4, 7831.
- [26] M. W. Jung, J. S. Lee, J. Koo, J. Park, Y. W. Song, K. Lee, S. Lee, J. H. Lee, *Opt. Express* **2014**, 22, 7865.
- [27] J. S. Lee, J. Koo, Y. M. Jhon, J. H. Lee, *Opt. Express* **2014**, 22, 6165.
- [28] J. D. Yao, G. W. Yang, *Small* **2018**, 14, 1704524.
- [29] J. D. Yao, J. M. Shao, Y. X. Wang, Z. R. Zhao, G. W. Yang, *Nanoscale* **2015**, 7, 12535.
- [30] A. Lawal, A. Shaari, R. Ahmed, N. Jarkoni, *Phys. Lett. A* **2017**, 381, 2993.
- [31] F. X. Liang, J. Z. Wang, Z. X. Zhang, Y. Y. Wang, Y. Gao, L. B. Luo, *Adv. Opt. Mater.* **2017**, 5, 1700654.
- [32] G. H. Zhang, H. J. Qin, J. Teng, J. D. Guo, Q. L. Guo, X. Dai, Z. Fang, K. H. Wu, *Appl. Phys. Lett.* **2009**, 95, 053114.
- [33] N. Zhou, Y. H. Shen, Y. Zhang, Z. Q. Xu, G. H. J. Zheng, L. Li, Q. Chen, H. P. Zhou, *Small* **2017**, 13, 1700484.
- [34] C. Xie, Y. Wang, Z. X. Zhang, D. Wang, L. B. Luo, *Nano Today* **2018**, 19, 41.

- [35] Y. B. Lee, J. Kwon, E. Hwang, C. H. Ra, W. J. Yoo, J. H. Ahn, J. H. Park, J. H. Cho, *Adv. Mater.* **2015**, 27, 41.
- [36] S. Friedensen, J. T. Mlack, M. Drndić, *Sci. Rep.* **2017**, 7, 13466.
- [37] B. Nie, J. G. Hu, L. B. Luo, C. Xie, L. H. Zeng, P. Lv, F. Z. Li, J. S. Jie, M. Feng, C. Y. Wu, Y. Q. Yu, S. H. Yu, *Small* **2013**, 9, 2872.
- [38] X. W. Tong, W. Y. Kong, Y. Y. Wang, J. M. Zhu, L. B. Luo, Z. H. Wang, *ACS Appl. Mater. Interfaces* **2017**, 9, 18977.
- [39] X. Hu, X. D. Zhang, L. Liang, J. Bao, S. Li, W. L. Yang, Y. Xie, *Adv. Funct. Mater.* **2014**, 24, 7373.
- [40] X. H. Liu, D. J. Yu, F. Cao, X. M. Li, J. P. Ji, J. Chen, X. F. Song, H. B. Zeng, *Small* **2017**, 13, 1700364.
- [41] S. F. Leung, K. T. Ho, P. K. Kung, V. K. S. Hsiao, H. N. Alshareef, Z. L. Wang, J. H. He, *Adv. Mater.* **2018**, 30, 1704611.
- [42] X. B. Xu, C. C. Chueh, P. F. Jing, Z. B. Yang, X. L. Shi, T. Zhao, L. Y. Lin, A. K. Y. Jen, *Adv. Funct. Mater.* **2017**, 27, 1701053.
- [43] V. Adinolfi, O. Ouellette, M. I. Saidaminov, G. Walters, A. L. Abdelhady, O. M. Bakr, E. H. Sargent, *Adv. Mater.* **2016**, 28, 7264.
- [44] N. Dong, X. W. Fu, G. Lian, S. Lv, Q. L. Wang, D. L. Cui, C. P. Wong, *ACS Appl. Mater. Interfaces* **2018**, 10, 8393.
- [45] W. B. Wang, D. W. Zhao, F. J. Zhang, L. D. Li, M. D. Du, C. G. Wang, Y. Yu, Q. Q. Huang, M. Zhang, L. L. Li, J. L. Miao, Z. Lou, G. Z. Shen, Y. Fang, Y. F. Yan, *Adv. Funct. Mater.* **2017**, 27, 1703953.